

An Exceptionally Stable and Widespread Hydrated Amorphous Calcium Carbonate Precipitated By the Dog Vomit Slime Mold *Fuligo Septica* (Myxogastria)

Laurence A.J. Garvie (✉ lgarvie@asu.edu)

Arizona State University

Péter Németh

Eötvös Loránd Research Network

László Trif

Institute of Materials and Environmental Chemistry, Research Center for Natural Sciences

Research Article

Keywords: amorphous calcium, ACC, XRD, TEM

Posted Date: November 30th, 2021

DOI: <https://doi.org/10.21203/rs.3.rs-1097298/v1>

License:  This work is licensed under a Creative Commons Attribution 4.0 International License.

[Read Full License](#)

Version of Record: A version of this preprint was published at Scientific Reports on March 7th, 2022. See the published version at <https://doi.org/10.1038/s41598-022-07648-9>.

Abstract

Biogenic amorphous calcium carbonate (ACC) is typically metastable and can rapidly transform through aging, dehydration, and/or heating to crystalline calcium carbonate. Gaining insight into its structure and properties is typically hampered by its tendency to crystallize over short time periods once isolated from the host organism, and also by the small quantities that are usually available for study. Here, we describe an exceptionally stable hydrated ACC (HACC) precipitated by the cosmopolitan slime mold, *Fuligo septica* (L.) F.H. Wigg. (1780). A single slime mold can precipitate up to one gram of HACC over the course of one night. Powder x-ray diffraction (XRD) patterns, transmission electron microscopy (TEM) images, infrared absorption (IR) spectra, and lack of optical birefringence are consistent with an amorphous material. XRD simulations supported by thermogravimetric (TG) and evolved gas analysis (EGA) data suggest an intimate association of organic matter with ~1-nm-sized ACC units that have monohydrocalcite- and calcite-like nano-structural properties. It is postulated that this association imparts the extreme stability of the HACC by preventing loss of H₂O and subsequent crystallization. The composition, structure, and thermal behavior of the HACC precipitated by *F. septica* collected over 8000 km apart, and in markedly different environments, suggests a common structure, as well as similar biochemical and biomineralization mechanisms for the HACC formation.

Introduction

Considerable work is ongoing with the view of understanding the structure of amorphous calcium carbonate (ACC), and the mechanisms by which it crystallizes¹⁻⁹. ACC is typically a transient material that transforms into crystalline calcium carbonate. For example, laboratory synthesized ACC can transform within minutes to vaterite and calcite¹⁰, and synthetic ACC free of stabilizing ions or organic molecules typically forms crystalline CaCO₃ within a few days^{11,12}. Biogenic ACC can be broadly divided into transient anhydrous ACC and comparatively more stable material with ~1 mol of water¹³⁻¹⁵. Biogenic and synthetic hydrated ACC typically contains about 1 mol H₂O. For example, synthetic ACC can contain between 1.13 to 1.58 moles of H₂O^{5,7,16}, with mass losses up to ~200° C similar to that measured for monohydrocalcite. Though, ACC has been synthesized with lower H₂O contents, e.g.^{5,17}. Characterization of ACC is challenging as it can be difficult to detect, in part because of its instability, and its presence may be masked by crystalline Ca carbonates.

ACC can be stabilized, or is metastable, in the presence of inorganic ions, including Mg²⁺ and phosphate, and organic molecules^{13,14,18-20}. For example, ACC produced by cave bacteria is stable in the presence of extracellular polysaccharides¹⁹. While the bacteria produce a wide range of organic molecules at their cell wall surface, the presence of large amounts of long-chain fatty acids suggests that the ACC could be enclosed in micellar-like units that inhibit water infiltration, and thus stabilize the ACC. Earthworms ACC can remain stable for years²¹. Its ACC contains high concentrations of amino acids, suggesting a stabilizing role of the organic compounds. Similarly, ACC from an ascidian skeleton contains

glycoproteins, with high concentrations of glutamic acid and hydroxy amino acids: these macromolecules are suggested to play a role in the stability of the ACC¹⁴.

Structural investigations of ACC suggest a range of short-range orderings, from vaterite-like¹, calcite-like^{1,3} and monohydrocalcite-like structures⁴, though others suggest that the short-range order is inconsistent with known calcium carbonate structures⁵. Despite these diverse viewpoints, the structural analyses for ACC universally suggest short-range order. For example, Ca EXAFS data is consistent with a structure lacking coherence above 1.5 nm⁵, suggesting that short-range order does not extend beyond the first coordination shell of Ca, which is about 0.4 nm from the central Ca atom⁴. Further, Sun et al.⁹ synthesized organic protected clusters of ACC with seven CaCO₃ units with an ~1.4 nm core. The ¹³C NMR and Ca K-edge EXAFS data demonstrate the rather disordered nature of the Ca sites with a mixture of Ca-O coordinations, geometries, and bond lengths. However, despite this disorder, the data suggest a proto-calcite-like short-range order. In contrast, Rez et al.⁸ proposed a nanocrystallite model for ACC consisting of randomly oriented 1-nm-sized nanocrystals with water molecules between the distorted nanocrystallites. This model is based on the idea of coherent x-ray diffraction from randomly oriented ~1-nm-sized crystallites, which gives rise to a diffraction profile that is characterized as amorphous. Goodwin et al.² developed a model for synthetic ACC consisting of a porous Ca-rich framework that supports interconnected channels containing water and carbonate molecules, though still lacking long-range order. These data, and those from other studies imply that not all ACC is the same²², i.e., there is unlikely a universal ACC structure.

A wide range of organisms precipitate ACC, including worms, mollusks, sponges, crustaceans, ascidia, bacteria, myxogastria, avian eggshells, and plants,^{14,19,21,23-26}. Particularly widespread, though less frequently studied, is the structure of the calcium carbonate precipitated by the myxogastria, a group of organisms commonly called slime molds²⁷⁻³¹. Study of slime mold carbonate is typically hampered by the small sizes of most species. However, some form cm- to dm-sized spore-filled masses called aethalia, which can be covered by a mineralized coating called a peridium³². Most notable are the aethalia produced by the cosmopolitan species *Fuligo septica*^{32,33}, which can be up to 75 cm across³³. The calcium carbonate precipitated by slime molds typically occurs as micron and submicron-sized spheres or euhedral crystals^{27,28,31,32,34-36}, though rarely is the precipitated material characterized, and is variously referred to as "lime", in the literature. For example, Schoknecht³⁰ employed a scanning electron microscope with x-ray microanalysis to study the calcareous deposits from a range of acellular slime molds: the presence of crystalline versus amorphous CaCO₃ was based on crystal shapes. There is evidence to suggest that the calcium carbonate precipitated by *F. septica* peridium is in part amorphous²⁸.

In this study, we describe and characterize the ACC formed by the cosmopolitan slime mold *F. septica* (L.) F.H. Wigg (1780)³⁷, commonly known as the dog vomit or scrambled-egg slime mold. The structure, characteristics, and composition of the freshly precipitated peridium is revealed using powder x-ray

diffraction (XRD), scanning and transmission electron microscopy (SEM and TEM), infrared spectroscopy (IR), thermal techniques (TG - thermogravimetric analysis, DSC - differential scanning calorimetry, and MS-EGA - mass spectroscopic evolved gas analysis), and bulk elemental analysis by proton-induced x-ray emission (PIXE) and CHN analysis. These techniques were also used to follow the laboratory dehydration of the as-precipitated, hydrous ACC (HACC) to a dehydrated form (DACC), and the crystallization to calcite. The sequence of transformations is HACC to DACC, which is stable to 322°C, crystallization of calcite between 322 and 440°C, and complete transformation to calcite by 450°C. A major finding of our study is that the *F. septica* HACC and DACC are indefinitely stable under normal laboratory conditions. Our data are consistent with an intimate association of organic matter with ~1-nm-sized ACC units that have monohydrocalcite- and calcite-like nano-structural properties. It is speculated that this association imparts the extreme stability of HACC by preventing loss of H₂O with subsequent crystallization.

Results And Discussion

Characterization of the field collected ACC. Aethalia from 37 *F. septica* specimens were collected (See Field Observations under Methods) and stored under normal laboratory conditions. The aethalia consists of an inner spore mass and an outer peridium. The peridium is the thin, to 3-mm thick, brittle porous coating that covers and surrounds the spore-bearing aethalium (Figs. 1a, b, S1c). The specimens from southern Arizona are white (referred to as FSW for **Fuligo Septica White**) and the UK specimens are bright lemon yellow (referred to as FSY) (Figs. 1, S1, S2). The yellow of the FSY specimens is caused by a range of pigmented compounds including the tetramic acid derivative fuligorubin A³⁸, which also acts as a metal chelating agent^{39,40}. Observations of the Arizona specimens by the senior author showed formation of the aethalium during the evening and early hours of the morning within a few days following summer rains. By morning, the aethalia are fully developed and samples were collected for study. Fragments of the peridia free of the spores were separated for analysis (Fig. S2).

A combination of PIXE, TG analysis, and CHN analysis were used to analyze the elemental composition of the FSY and FSW peridia (Tables 1, S1, S2). Calcium is the major cation. The FSY samples contain ~3.3 wt% Mn, whereas the FSW samples contain between 937 and 2186 ppm Mn. Magnesium was typically at or below the PIXE detection limit of ~200 ppm: the only other elements consistently above the limit of detection for the PIXE are P, S, Cl, and K (Table S1).

Optical, SEM, and TEM images show the peridia composed of 500- to 1500-nm-sized spheres (Figs. 1, 2, S1d), consistent with previous SEM images²⁸. The spheres are isotropic under crossed polarized transmitted light (Fig. 1f). The high-angle annular dark-field scanning TEM (HAADF-STEM) and bright-field TEM (BFTEM) images show that the spheres typically have an internally mottled appearance. This mottling is especially evident in the BFTEM images, which show rounded, 20- to 40-nm-sized electron dense units (Figs. 2c and S3). The selected-area electron diffraction (SAED) patterns of the spheres show diffuse rings (Fig. 2d), similar to what was reported by Enyedi et al.¹⁹ for bacterially precipitated ACC.

Multiple peridial samples were examined by powder XRD: all lack the sharp intense Bragg reflections of crystalline phases, and are instead dominated by five broad, but well-defined maxima at ~ 1.9 , 0.46 , 0.2866 , 0.204 nm, 0.119 nm, and weak maxima at higher d-spacings (Fig. 3). The high signal-to-noise ratio of our powder XRD patterns, compared with published data, was possible because of the large amount of pure HACC produced by the slime mold, and its exceptional stability in air. For example, the XRD patterns of the FSW and FSU samples acquired within hours of formation compared with those stored in the laboratory for two years are identical. Except for the ~ 1.9 nm reflection, the diffraction patterns are similar to those for synthetic and biogenic ACC^{5,7,26,41-43}. The prominent ~ 1.9 nm has not previously been reported and suggests ordering at the ~ 2 nm scale.

The FTIR spectra of the HACC (Figs. 4, S4, S5) show the characteristic bands of ACC, with spectra similar in shape to biogenic (e.g., Fig. 2a and b, and in Addadi et al.²³) and synthetic ACC (Radha et al.⁷ supplement). The FSU and FSW HACC spectra lack the distinctive ν_4 band for crystalline CaCO_3 , i.e., 712 cm^{-1} for calcite and 744 cm^{-1} for vaterite. Instead, the HACC spectra display low-intensity bands at 727 and 693 cm^{-1} that sit on a broad band centered near 600 cm^{-1} . The IR spectrum shows the broad band between $2750\text{-}3800\text{ cm}^{-1}$ from absorbed and structural water, on which are superimposed weak absorption bands for organic material (inset Fig. S4). In comparison to the amorphous HACC, aged samples collected in the desert show FTIR spectra with characteristic absorption bands for crystalline CaCO_3 (Figs. S4, S5).

The moisture stability of the FSU and FSW samples was investigated by placing the XRD slide with the sample used for powder XRD into a sealed container over water at 50°C for 24 hrs. The sample became damp over the 100% RH and a new powder XRD pattern was acquired. The FSU ACC diffraction pattern was unchanged, even after several 24 hr sessions of the 100% RH treatment. However, the FSW ACC showed the appearance of calcite reflections after one 24 hr session of 100% RH. These reflections became more intense with each 24 hr sessions of 100% RH, though no reflections for vaterite were noted (Fig. S6). In contrast, FSW samples collected after weeks to months of natural desert weathering are dominated by vaterite with minor calcite, to those dominated by calcite with minor vaterite: one peridium is composed of monohydrocalcite with minor amounts of calcite (Fig. S7).

Thermal response. The TG curves for the ACC samples studied under a He atmosphere show four distinct mass-loss steps, M1 to M4 (Figs. 5, S8, S9). The total mass losses for the FSW and FSU samples heated to 1000°C were typically between 52 and 57%. The DSC curves show an endothermic peak at $\sim 100^\circ\text{C}$, corresponding to dehydration of the HACC and loss of loosely bound water (Fig. 5). The TG loss below 200°C is between 10.5 and 10.9% for the FSW samples (samples FSW21 and FSW18) and 11.2% for FSU. The EGA ion curves show that the mass loss below 200°C is dominated by the evolution of H_2O with minor CO_2 (Fig. 5, S10, S11). In region M2, the mass loss is dominated by H_2O (3.8%), CO_2 (Fig. S11) and organic molecules (Fig. S10d): the intense $m/z=30$ signal matches that of formaldehyde (see caption to Fig. S10 for additional ion peak assignments). During the M3 mass-loss step (between 396 and 584°C), organic matter is pyrolytically degraded (Fig. S12), with the evolution of a range of organic-bearing

species, with minor H₂O and CO₂ (Fig. S10). Above 584°C, calcium carbonate decomposes, and the ion signals are dominated by m/z=44 corresponding to CO₂ (Figs. 5, S10).

Quantity of water and organic matter. The FSY and FSW HACC shows TG mass losses up to 200°C of ~11 wt%, the majority of which is H₂O. For example, of the 11.2% mass loss for FSY below 200°C (Fig. S11), 10.9±0.1% is from H₂O, and the rest is CO₂ (see Supplementary section - Water Calculation from TG-DSC-MSEGA measurements). A further 3.8% H₂O is released in region M2 (Fig. S11), though only 3.0% up to the crystallization temperature onset at 322°C (see discussion below). However, considering the composition of the FSY HACC as inorganic Ca-C-O-O-O-H-H-O (equivalent to monohydrocalcite: CaCO₃·H₂O) + remaining C-H-N-O, then 13.72 wt% water loss (corresponding to 1 mole of water) is expected (Tables S3, S4). The lower-than-expected amount of water released below 200°C for FSY, i.e., 1CaCO₃:nH₂O ratio with n<1, may indicate significant molecular H₂O retained above 200°C, but released before and during crystallization of the ACC starting near 322°C. Such a scenario is borne out by the TG data which shows a total H₂O release up to 322°C of 13.9%. While the low-temperature water-loss peak has a maximum just above 100°C, which then drops precipitously with a plateau near 200°C, H₂O continues to be released with increasing temperature and peaks near 320°C, with little H₂O detected above 400°C (Figs. S10a, S11). These data suggest that the water released between 200 and 320°C has several sources including molecular H₂O and that bound to the organic compounds.

The FTIR spectra show weak absorption bands between 2800 and 3000 cm⁻¹ attributed to organic matter associated with the HACC (Fig. S4). The breakdown of this organic matter is also detected by EGA during heating of the HACC (Fig. S10). Samples heated in air have a higher mass loss than those heated under an inert atmosphere (Fig. S13). For example, FSY shows higher mass losses when heated in air between 200 and 575°C. In this temperature range, 19% of the mass is lost in the case of samples measured in air, and 15.1% when heated under He. This ~4% difference sets a minimum in the FSY sample on the organic content as some is pyrolytically degraded under He. The quantity of organic matter can also be estimated from the compositional data (Tables 1, S3 to S6). Assuming an inorganic formula for FSY as (Ca,Mn)₁CO₃·H₂O, then the remainder is assumed to be organic and has the composition C_{0.60}O_{0.09}H_{1.41}N_{0.14}, which is 9.13% of the original HACC mass (Tables S3, S4). Similarly, the composition for FSW21 (Table 1) suggests it contains 9.83% organic matter (Tables S5, S6). Thus, the TG data is consistent with the *F. septica* HACC containing between approximately 4 and 10% organic matter.

Despite the elemental and compositional similarities between the *F. septica* HACC and monohydrocalcite (Table 1), their thermal behaviors differ significantly. Monohydrocalcite typically dehydrates by 226°C, with mass loss of 15.25% H₂O, corresponding to CaCO₃·H₂O → CaCO₃ + H₂O, and 37.26 wt% mass loss above 530°C for CaCO₃ → CaO + CO₂^{44,45}. Monohydrocalcite shows minimal mass loss below ~180°C, and between ~200 and 500°C. In contrast, the slime mold ACC shows significant mass loss below 180°C, and also between 200 and 500°C. The slime mold thermal data are consistent with the different H environments, similar to that detected in ACC by Nuclear Magnetic Resonance spectroscopy¹⁶, viz., fluid-

like H₂O, rigid structural H₂O, restrictedly mobile H₂O, and hydroxyl. Our mass loss up to 200°C is dominated by the loss of fluid-like H₂O.

Laboratory crystallization of the DACC. The powder XRD data show onset of crystallization of the DACC between 300 and 350°C (Fig. S14). Similarly, SAED patterns and FTIR spectra of the HACC heated at 208°C show an amorphous material, but at 362°C the patterns and spectra show partial crystallization, and at 500°C the spheres are calcite (Fig. S15 to S17). At 362°C, the BFTEM images show that the newly formed calcite is ~40 nm, which is similar in size to the electron-dense aggregates imaged by BFTEM in the nanospheres (Fig. 2c, S3). By 500°C, the 40-nm nano-objects have organized into micron-sized grains and form calcite (Fig. S15). The spherical morphology is preserved during the transition (Fig. S15). Individual spheres show sharp extinction when rotated between the crossed polars, indicating that each is a single crystal and preserves the original spherical morphology.

The DSC profiles for HACC samples examined under He show peaks for exothermic reactions between 300 and 480°C (Fig. 5). The FSU sample shows prominent maxima at 327 and 401°C in the raw thermogram. Most of the FSW samples similarly reveal two well-resolved exothermic maxima near 338 and 414°C (Fig. S18). One sample (FSW21) lacks the 338°C maximum. The EGA data show a maximum in the evolution of a range of gases just prior to the first exotherm maximum for both the FSU (Fig. 6) and FSW (Fig. S19) precipitated HACC. Many of the gases associated with organic molecules show a two-peaked evolution with maxima at ~260 and ~320°C, whereas water and CO₂ show a more gradual increase in signal intensity starting around 240°C, with a maximum near 320°C. The first exotherm between 327 and 338°C is within the crystallization range identified by powder XRD, and previously attributed to the crystallization of the dehydrated ACC^{7,17,41,46}, although this maximum can occur over a range of temperatures¹⁶. Some biogenic ACCs show two exothermic peaks in the 330 to 370°C range⁴⁷. For example, the “Gastrolith ACC 2” DSC curve from⁴⁷ shows two exothermic peaks, of which one may be attributed to the breakdown of chitin⁴⁸. Between the first and second exotherm, the slime mold ACC continues to lose mass, typically between 1.3 and 3.5 wt%. However, additive free ACC does not typically show mass loss following the exothermic event near 340°C, indicating a solid-state transformation to calcite as no remaining water is available^{7,17}.

Our data suggests the breakdown of an organic framework to the DACC starting near 240°C, culminating with a maximum in several EGA signals just prior to the first DSC exotherm, with partial crystallization. The powder XRD data for the sample at 350°C still shows a significant amorphous contribution (Fig. S14). By 365°C, the powder XRD pattern shows intense reflections for calcite that sit on a less intense amorphous ACC background. Optical microscopy shows that at 365°C, approximately 20% of the spheres are isotropic. The DSC maximum near 400°C likely corresponds to the onset of crystallization of the remainder of the as yet amorphous part of the ACC, as optical microscopy and powder XRD of samples heated at 446°C show calcite only.

Multi-scale structure of the HACC. Our data for the *F. septica* HACC is consistent with the following structural spatial scales, viz., 1) the 500- to 1500-nm-sized sphere; 2) tens-of-nanometer-sized clumping

within the spheres; 3) an ~2-nm-scale ordering as revealed by the powder XRD; and, 4) the short-range ordering that gives rise to the bulk powder XRD pattern. Some of the structural characteristics of the HACC may be explained by the formation mechanisms of the individual spheres. Electron microscopy shows the aggregation and excretion of calcium during sporogenesis in the slime mold *Physarella oblonga*²⁷, which is in the same family as *F. septica*, the Physaraceae⁴⁹. As the slime mold transforms from the mobile plasmodium to the sessile fruiting body there is a massive elimination of the protoplasmic Ca. During sporogenesis, electron microscopy reveals the formation and aggregation of tens-of-nanometers–sized Ca-rich, electron-dense, membrane-bound intracellular grains. These grains aggregate and assume their final spherical shape as they grow and are expelled and form the peridium²⁷. This membrane-bound aggregate model is consistent with our BFTEM of the *F. septica* spheres, which internally show tens-of-nanometer-scale electron-dense clumping (Figs. 2c, S3). However, the aggregates themselves are amorphous as the powder XRD profiles do not show reflections indicative of crystalline ordering at the tens-of-nanometer scale (Fig. S21).

The origin of the ~1.9 nm powder XRD maximum is obscure. This maximum becomes indistinct, or is absent, for samples heated to ~100°C, or stored over the aggressive drying agent P₂O₅. Thus, the 1.9 nm maximum may reflect ordering at this scale that is absent after loss of the weakly bound water. Ordered mesoporous material can give rise to low-angle maxima that reflect the pore-to-pore distance as well as the pore diameter⁵⁰. Thus, the ~1.9 nm maximum suggests an ordered mesoporous structure to the *F. septica* HACC that is readily lost on removal of the loosely bound water.

The powder XRD patterns for the room temperature and heated *F. septica* ACC lack discrete reflections for crystalline phases, and instead present broad maxima that reflect the short-range order within the spheres. These maxima represent the average interatomic distance scattering within the material and are indicative of short-range order. Rez et al.⁸ show a strong match between the SAED patterns from synthetic and biogenic ACC and calculated patterns for random packing of ~1-nm-sized calcite crystals. Similarly, we compare the powder XRD patterns for the *F. septica* HACC with the simulated scattering profiles for ~1-nm-sized particles of anhydrous and hydrated CaCO₃ polymorphs (Fig. 7, S20). Only the simulated pattern for monohydrocalcite shows four oscillations that match the 0.46, 0.2866, 0.204, and 0.119 nm maxima for the *F. septica* HACC powder XRD patterns. The simulated pattern for monohydrocalcite further shows a weak oscillation near 0.1467 nm which, if present in the experimental pattern, is obscured by the tail of the intense 0.288 nm peak. However, the 0.2866 nm peak in the experimental pattern is considerably more intense than the corresponding peak in the simulated pattern for monohydrocalcite. The intensity of this peak can be simulated by assuming an HACC structure with both monohydrocalcite and calcite like nano-structural ordering (Fig. 7). The main maximum for the HACC at 0.2866 nm is at a higher d-spacing than that predicted by the simulations. A similar situation was shown between the calculated patterns for calcite and biogenic calcite, which Rez et al.⁸ attributed to the contraction of the nanocrystals relative to the bulk calcite. The simulations lend support to a structure composed of ~1-nm-sized diffracting domains, as the simulated patterns change dramatically

just by doubling the particle size, with sharpening of the maxima and appearance of new peaks that are not present in the experimental patterns (Fig. S21).

Conclusions

The powder XRD, electron diffraction, IR data, and lack of optical birefringence are consistent with the *F. septica* HACC spheres as an amorphous material with sub-nanometer-sized diffracting domains. The XRD simulations are consistent with an HACC that possesses short-range structure with both monohydrocalcite- and calcite-like nano-structural properties, possibly reflecting a range of coordination environments from six to eight O around the Ca. The EGA data are consistent with the breakdown of an organic framework to the DACC starting near 240°C, culminating with a maximum in several EGA signals just prior to the first DSC exotherm, with partial crystallization. Together, the powder XRD, EGA, and elemental data suggest a structure dominated by ~1-nm-sized monohydrocalcite- calcite-like units separated by organic material. Further, the ~2-nm-sized spacings present in the HACC XRD patterns suggest ordering at this scale that is disrupted as the mobile water is released. Previous work on ACC suggests that crystallization occurs from an intermediate anhydrous ACC. However, the slime mold DACC is not strictly anhydrous as ~3 wt% water is released after the loss of the loosely bound water and before the first crystallization exotherm. This water loss is supported by the IR spectra that still show strong broad H₂O FTIR absorption bands after heating to 208°C.

The transformation and crystallization of the *F. septica* HACC by laboratory heating differs significantly from that observed in naturally weathered samples collected in the desert. Many examples of *F. septica* collected within days to months after their formation in the desert were vaterite rich, with one dominated by monohydrocalcite. These mineralogical differences suggest that the crystallization mechanism(s) via laboratory heating versus natural weathering are not the same. In the desert environment, the peridial ACC, which sits on the ground, will experience significant diurnal temperature and humidity variations⁵¹: these variations could drive the reorganization of the ACC into different crystalline anhydrous or hydrous calcium carbonates. These data suggest that the transformation pathway is not necessarily pre-determined by the initial HACC structure, but instead by environmental or laboratory conditions, a conclusion consistent previous findings¹⁷.

A major finding of our study is that the ACC precipitated by the slime mold *F. septica* is indefinitely stable under normal laboratory conditions. We propose that the intimate association of the organic matter with ~1-nm-sized ACC units prevents its crystallization. The composition, structure, and thermal behavior of the HACC precipitated by *F. septica* collected over 8000 km apart, and in markedly different environments, suggests a common structure, as well as similar biochemical and biomineralization mechanisms for the HACC formation.

Experimental Section

Field observations. *Fuligo septica* is a cosmopolitan species³⁷. Specimens collected in southern Arizona are commonly found after summer rains. The author observed specimens from the arid parts of southwestern Arizona to the more mesic mountain regions in the eastern part of the state. It is locally abundant, for example 103 aethalia were counted in a 15 x 5 m area (33°16'33.14"N, 111° 9'57.25"W, August 2018) under mesquite trees. Several hundred aethalia were found amongst perennial bushes and trees along a 1 km stretch of a dry wash (33° 1'58.15"N, 112°14'35.99"W, July 2017) southwest of Phoenix. The plasmodium emerges from the damp ground during the relative cool of the night and moves to an exposed position where it forms an aethalium. By morning, the aethalium is fully formed. The aethalia are typically pulvinate, 3 to 15 cm in diameter, and 2 cm thick. A cross section of the aethalium shows a dome-shaped peridium of white, soft, chalky material coating the spore mass (Fig. S1). The peridium and spore mass sit on the hypothallus. The peridium from eight separate aethalia of *F. septica* were collected during June 2018 in Highgate Woods, London (51°35'0.38"N, 0°8'59.42"W). The aethalia are pulvinate, bright canary yellow, with the largest to 7 cm. The cortex is up to 3 mm thick and separated easily from the spore mass. The aethalia were all whole and undisturbed and it is estimated that they were collected within a few days of having formed. The Arizona and UK specimens studied here match the description for *F. septica* in³⁷.

Separation of the ACC. The peridium from the Arizona (FSW) aethalia was easiest to collect from the still-moist samples soon after collecting in the early morning. The white but damp peridium has a consistency of whipped cream cheese, which is easy to collect with a small spatula from the edge of aethalia. In this way, up to 200 mg of pure, dried ACC could be separated from a single aethalia. The peridium can also be collected from the dry aethalia, although care is needed so as to not incorporate the underlying spores in the sample. In contrast, the peridium from the UK (FSY) samples separated easily from the spore mass as porous yellow chunks up to 1 cm across (Fig. S2).

Powder X-ray diffraction and simulations. Powder XRD patterns were acquired with a Rigaku MiniFlex 600 diffractometer. This diffractometer is operated with Cu *K* α radiation and is equipped with a post-diffraction graphite monochromator and automatic divergence slit system. Data was typically acquired in step scan mode at 0.02° steps, and 30 to 60 s/step. Samples, typically weighing ~10 mg, were mixed with a small drop of methanol forming a slurry. The resulting slurry was pipetted and spread into a thin, smooth film on a low-background, single-crystal, quartz plate. This slurry was dried rapidly (~5 s) under blowing warm air forming a thin film. In order to demonstrate that the methanol treatment did not affect the shape of the XRD profile, a sample was run as a dry powder sprinkled onto the quartz plate. The XRD pattern from the dry powder pattern and the thin film formed from the slurry were identical, showing that the methanol does not affect the slime mold HACC structure. Samples, weighing ~ 40 mg each, were heated at 150°, 300°, 350°, and 500° C in air for ½ hr, and two samples of ~20 mg were heated at 365 and 446°C under flowing He for ½ hr. The specific heating temperatures were guided by the dominant changes observed in the TG-DSC data. The heated samples were deposited onto the quartz plate and the XRD pattern initially acquired rapidly (1/2 hr) and then over an extended time period (20 hrs) to ensure that

initially heated material remained stable. Samples were also periodically rerun over the course of months to two years to check for changes in the overall shape of the diffraction patterns.

Simulated patterns were calculated with the CrystalDiffract software by CrystalMaker Software Ltd. Patterns were calculated assuming Gaussian profiles, particle sizes were varied as shown in the figures and Iso strain was set to 0%. Ideal lattice parameters were used for the simulations and site occupancies were set at 100%.

TG-DTA/DSC. Thermal measurements were performed on a Setaram LabsysEvo (Lyon, France) TG-DTA/DSC system, in flowing (60 mL/min) purging gas atmosphere [99.9999% purity He /DTA/, 99.999% purity Ar /DSC/ and 99.999% purity synthetic air (20% O₂ in N₂) /DSC/ atmospheres]. The sample was weighed into a 100 µL Al₂O₃ crucible (the reference crucible was empty) and heated from 25°C to 1000°C with a heating rate of 10°C/min. Two measurements were done in one type of gas, one with a smaller amount of mass (~10 mg) and another one with a larger sample mass (~35 mg) in order to enhance the effects on the heat flow signal. The obtained data was baseline corrected and further processed with the thermoanalyzer's processing software (Calisto Processing, ver. 2.092). The thermal analyzer (both the temperature scale and calorimetric sensitivity) was calibrated by a multipoint calibration method, in which seven different certified reference materials (CRM's) were used to cover the thermal analyzer's entire operating temperature range.

TG-DSC-MSEGA. Thermal measurements were performed on a Setaram LabsysEvo (Lyon, France) TG-DSC system, in flowing (90 mL/min) helium gas (99.9999% purity) atmosphere. The sample was weighed directly into a 100 µL Al₂O₃ crucible (the reference cell was empty) and was heated from 25°C to 1000°C with a heating rate of 20°C/min. The obtained data was baseline corrected and further processed with the thermoanalyzer's processing software (Calisto Processing, ver. 2.092). The thermal analyzer (both the temperature scale and calorimetric sensitivity) was calibrated by a multipoint calibration method, in which seven different certified reference materials (CRM's) were used to cover the thermal analyzer's entire operating temperature range. In parallel with the thermal measurements, the analysis of evolved gases/volatiles was performed on a Pfeiffer Vacuum Omni Star™ mass spectrometric evolved gas analysis system (MS-EGA), which was connected to the above-mentioned thermal analyzer. The gas splitter was thermostated to 230°C, while the transfer line to the mass spectrometer was thermostated to 220°C. The temperature of the mass spectrometer gas inlet was programmed to 120°C. The measurements were done in SEM Bargraph Cycles acquisition mode, where the m/z interval of 11-130 was continuously scanned with a speed of 50 ms/amu. The spectrometer was operated in electron impact mode. The amount of "free" water was calculated by comparing the corresponding areas between room temperature and 200°C from two standard calibration materials (calcium oxalate monohydrate and potassium bicarbonate) adapted from the work of ⁵².

FTIR spectroscopy. FTIR measurements were recorded on a Jasco FT/IR-4600 (Japan) system, equipped with a Jasco ATR Pro One single reflection diamond ATR (attenuated total reflection) accessory (incident angle 45°), and a mid-range MCT (Mercury-Cadmium-Telluride) detector. A spectral resolution of 4 cm⁻¹

and co-addition of 128 individual spectra were applied. Prior to the evaluation, an ATR correction (Jasco Spectra Manager version 2, Spectra analysis module version 2.15.11) was performed on the raw spectra.

Scanning and transmission electron microscopy. Dry precipitates of the *Fuligo septica* HACC were gold coated and imaged with a ZEISS EVO 40 scanning electron microscope operated at 5 keV. TEM data were acquired with a 200 keV Talos Thermo Scientific transmission electron microscope. Grains of the pristine material and samples heated at 208°, 361°, and 500° C in an inert atmosphere for ½ hr were crushed under ethanol and deposited onto copper grids covered by lacey carbon. We obtained BFTEM, and HAADF-STEM images as well as SAED patterns. The elemental composition of the grains was measured with a “Super-X” detector system having four silicon drift detectors built into the microscope column.

Proton-induced x-ray emission. Nondestructive elemental analysis of slime mold ACC was undertaken by proton-induced x-ray emission (PIXE) spectroscopy. Proton beams were accelerated at low energy (1.90 MeV), with a 1.7 MeV Tandetron tandem accelerator (Cockroft-Walton type manufactured by General Electric). The proton beam of 1 x 1 mm crosses a 7.8-micron-thick kapton foil window before entering the sample chamber and striking the sample. The sample chamber is evacuated to low vacuum to avoid air signal and x-ray absorption. A Canberra Si(Li) detector (detector resolution at the 5.9 keV line is 168.0 eV) is placed at 47° from the normal of the sample surface, which is oriented at 45° with respect to the incoming proton beam. No filters were used in front of the detector for the low-energy, light-element analyses. The proton current incident on the sample was adjusted to ~0.5 nA.

PIXE was used to measure element concentrations of atomic number 11 (sodium) and greater. The spectra were acquired from areas ~1 x 1 mm on pressed 2-mm-diameter discs of ACC. Each spectrum was acquired for a total of 10,000 counts. The PIXE data were processed with the GUPIX software (www.physics.uoguelph.ca/PIXE, updated 2005). For standardization the instrumental constant H (solid angle and correction factor) is determined using the GUPIX database (cross-sections, fluorescence and Coster–Kronig probabilities, stopping powers and attenuation coefficients) for the range of element in the NIST biological reference material Bovine Liver (SRM-1577) and whewellite. The bovine standard was run and H determined prior to each ACC analysis. The C-H-N elemental data for the ACC (see below) were used to define the matrix for the GUPIX calculations.

CHN analysis. Bulk carbon, hydrogen, and nitrogen were determined using a Perking Elmer 2400 Elemental Analyzer in the Metals, Environmental and Terrestrial Analytical Laboratory at Arizona State University. Approximately 5 mg of powder was used for each analysis. The samples were loaded into tin cups and flash heated to 1760°C. The resulting gases were chemically scrubbed of the halogens and S and separated in a GC column. Detection is conducted by a thermal conductivity detector.

Declarations

Acknowledgements

L.G. was funded in part by an ASU Investigator Incentive Award (IIA# PG04789 CC0487). The research was also supported in part by the Ministry of Innovation and Technology of Hungary from the National Research, Development and Innovation Fund (projects FK141842, ANN141894 and NKFIH-872) and the Eötvös Loránd Research Network (NANOCARB project, SA-41/2021). We acknowledge the use of facilities within the Eyring Materials Center at Arizona State University supported in part by NNCI-ECCS-1542160. The authors are grateful to the following in the Eyring Materials Center for their assistance: PIXE (Barry Wilkens and Mark Mangus Jr), TG-DSC (Timothy Karcher and Xin Guo), and FTIR (Emmanuel Soignard), and to Cathy Kochert in the Metals, Environmental and Terrestrial Analytical Laboratory (METALS) at Arizona State University for help in measuring the CHN data. We are grateful to the staff and for the use of the Nanolab facility in the University of Pannonia.

Author contributions

L.G initiated the project. L.T. and L.G. measured the thermal and FTIR data. P.N. measured the TEM and SEM data. L.G acquired the XRD data. L.G. took the lead on the manuscript writing. All authors contributed substantially to all aspects of the data analysis and manuscript writing. All authors approved the manuscript.

Competing interests

The authors declare no competing interests.

References

1. Gebauer, D. *et al.* Proto-calcite and proto-vaterite in amorphous calcium carbonates. *Angew. Chem. Int. Ed*, **49**, 8889–8891 (2010).
2. Goodwin, A. L. *et al.* Nanoporous structure and medium-range order in synthetic amorphous calcium carbonate. *Chemistry of Materials*, **22**, 3197–3205 (2010).
3. Günther, C., Becker, A., Wolf, G. & Epple, M. In vitro synthesis and structural characterization of amorphous calcium carbonate. *Zeitschrift für anorganische und allgemeine Chemie*, **631**, 2830–2835 (2005).
4. Levi-Kalisman, Y., Raz, S., Weiner, S., Addadi, L. & Sagi, I. X-Ray absorption spectroscopy studies on the structure of a biogenic “amorphous” calcium carbonate phase. *Journal of the Chemical Society, Dalton Transactions*, 3977–3982 (2000)
5. Michel, F. M. *et al.* Structural characteristics of synthetic amorphous calcium carbonate. *Chemistry of Materials*, **20**, 4720–4728 (2008).
6. Politi, Y. *et al.* Transformation mechanism of amorphous calcium carbonate into calcite in the sea urchin larval spicule. *Proceedings of the National Academy of Sciences* **105**, 17362–17366 (2008)
7. Radha, A., Forbes, T. Z., Killian, C. E., Gilbert, P. & Navrotsky, A. Transformation and crystallization energetics of synthetic and biogenic amorphous calcium carbonate. *Proceedings of the National*

- Academy of Sciences* **107**, 16438-16443 (2010)
8. Rez, P., Sinha, S. & Gal, A. Nanocrystallite model for amorphous calcium carbonate. *Journal of Applied Crystallography*, **47**, 1651–1657 (2014).
 9. Sun, S., Chevrier, D. M., Zhang, P., Gebauer, D. & Cölfen, H. Distinct Short-Range Order Is Inherent to Small Amorphous Calcium Carbonate Clusters (< 2 nm). *Angew. Chem. Int. Ed*, **55**, 12206–12209 (2016).
 10. Shen, Q. *et al.* Properties of amorphous calcium carbonate and the template action of vaterite spheres. *The Journal of Physical Chemistry B*, **110**, 2994–3000 (2006).
 11. Lee, H. S., Ha, T. H. & Kim, K. Fabrication of unusually stable amorphous calcium carbonate in an ethanol medium. *Materials Chemistry and Physics*, **93**, 376–382 (2005).
 12. Rodriguez-Blanco, J., Shaw, S. & Benning, L. G. How to make 'stable'ACC: protocol and preliminary structural characterization. *Mineral. Mag*, **72**, 283–286 (2008).
 13. Aizenberg, J., Addadi, L., Weiner, S. & Lambert, G. Stabilization of amorphous calcium carbonate by specialized macromolecules in biological and synthetic precipitates. *Adv. Mater*, **8**, 222–226 (1996).
 14. Aizenberg, J., Lambert, G., Weiner, S. & Addadi, L. Factors involved in the formation of amorphous and crystalline calcium carbonate: a study of an ascidian skeleton. *Journal of the American Chemical Society*, **124**, 32–39 (2002).
 15. Raz, S., Hamilton, P. C., Wilt, F. H., Weiner, S. & Addadi, L. The transient phase of amorphous calcium carbonate in sea urchin larval spicules: the involvement of proteins and magnesium ions in its formation and stabilization. *Adv. Funct. Mater*, **13**, 480–486 (2003).
 16. Schmidt, M. P., Illott, A. J., Phillips, B. L. & Reeder, R. J. Structural changes upon dehydration of amorphous calcium carbonate. *Crystal growth & design*, **14**, 938–951 (2014).
 17. Konrad, F., Gallien, F., Gerard, D. E. & Dietzel, M. Transformation of amorphous calcium carbonate in air. *Crystal growth & design*, **16**, 6310–6317 (2016).
 18. Bentov, S., Weil, S., Glazer, L., Sagi, A. & Berman, A. Stabilization of amorphous calcium carbonate by phosphate rich organic matrix proteins and by single phosphoamino acids. *Journal of structural biology*, **171**, 207–215 (2010).
 19. Enyedi, N. T. *et al.* Cave bacteria-induced amorphous calcium carbonate formation. *Scientific reports*, **10**, 1–12 (2020).
 20. Gago-Duport, L., Briones, M., Rodríguez, J. & Covelo, B. Amorphous calcium carbonate biomineralization in the earthworm's calciferous gland: pathways to the formation of crystalline phases. *Journal of structural biology*, **162**, 422–435 (2008).
 21. Hodson, M. E. *et al.* Biomineralisation by earthworms—an investigation into the stability and distribution of amorphous calcium carbonate. *Geochemical transactions*, **16**, 1–16 (2015).
 22. Levi-Kalisman, Y., Raz, S., Weiner, S., Addadi, L. & Sagi, I. Structural differences between biogenic amorphous calcium carbonate phases using X-ray absorption spectroscopy. *Adv. Funct. Mater*, **12**, 43–48 (2002).

23. Addadi, L., Raz, S. & Weiner, S. Taking advantage of disorder: amorphous calcium carbonate and its roles in biomineralization. *Adv. Mater*, **15**, 959–970 (2003).
24. Benzerara, K. *et al.* The gammaproteobacterium *Achromatium* forms intracellular amorphous calcium carbonate and not (crystalline) calcite. *Geobiology*, **19**, 199–213 (2021).
25. Rodríguez-Navarro, A. B., Marie, P., Nys, Y., Hincke, M. T. & Gautron, J. Amorphous calcium carbonate controls avian eggshell mineralization: a new paradigm for understanding rapid eggshell calcification. *Journal of structural biology*, **190**, 291–303 (2015).
26. Setoguchi, H., Okazaki, M. & Suga, S. in *Origin, evolution, and modern aspects of biomineralization in plants and animals* 409–418 (Springer, 1989).
27. Bechtel, D. & Horner, H. Calcium excretion and deposition during sporogenesis in *Physarella oblonga*. *Calcified tissue research*, **18**, 195–213 (1975).
28. Chapman, C. P., Nelson, R. K. & Orlowski, M. Peridium of the acellular slime mold *Fuligo septica*: Structure and composition. *Exp. Mycol*, **6**, 195–199 (1982).
29. Lado, C. & Eliasson, U. Taxonomy and systematics: current knowledge and approaches on the taxonomic treatment of Myxomycetes. *Myxomycetes*, 205–251 (2017)
30. Schoknecht, J. D. SEM and X-ray microanalysis of calcareous deposits in myxomycete fructifications. *Transactions of the American Microscopical Society*, 216–223 (1975)
31. Schoknecht, J. D. & Keller, H. W. in *Origin, Evolution, and modern aspects of biomineralization in plants and animals* 455–488 (Springer, 1989).
32. Keller, H. W., Everhart, S. E. & Kilgore, C. M. in *Myxomycetes* 1-45 (Elsevier, 2022)
33. Keller, H. W., O'Kennon, B. & Gunn, G. in *Fun.* 6-11 (Fun)
34. Nelson, R. K. & Orlowski, M. Hypothallus of the acellular slime mold *Fuligo septica*: Structure and composition. *FEMS Microbiology Letters*, **18**, 83–87 (1983).
35. Yajima, Y., Hoshino, T., Kondo, N. & Chang, Y. C. Fruiting body formation of the nivicolous myxomycete *Badhamia alpina* in moist chamber culture. *Mycoscience*, **59**, 268–276 (2018).
36. Zhang, J., Liu, L., Fiore-Donno, A. M. & Xu, T. Ultrastructural characters of a *Physarum melleum* on living leaves of *Dendrobium candidum* in China. *Journal of Zhejiang University SCIENCE B*, **8**, 896–899 (2007).
37. Martin, G. W. & Alexopoulos, C. J. *The myxomycetes* (University of Iowa Press, 1969).
38. Casser, I., Steffan, B. & Steglich, W. The chemistry of the plasmodial pigments of the slime mold *Fuligo septica* (Myxomycetes). *Angewandte Chemie International Edition in English*, **26**, 586–587 (1987).
39. Setälä, A. & Nuorteva, P. High metal contents found in *Fuligo septica* (L.) wiggers and some other slime molds (Myxomycetes). *Karstenia*, **29**, 37–44 (1989).
40. Zaghouni, M. & Nay, B. 3-Acylated tetramic and tetric acids as natural metal binders: myth or reality? *Natural product reports*, **33**, 540–548 (2016).

41. Koga, N. & Yamane, Y. Thermal behaviors of amorphous calcium carbonates prepared in aqueous and ethanol media. *Journal of Thermal Analysis and Calorimetry*, **94**, 379–387 (2008).
42. Sun, R. *et al.* Amorphous calcium carbonate constructed from nanoparticle aggregates with unprecedented surface area and mesoporosity. *ACS applied materials & interfaces*, **10**, 21556–21564 (2018).
43. Wang, Y. Y., Yao, Q. Z., Zhou, G. T. & Fu, S. Q. Transformation of amorphous calcium carbonate into monohydrocalcite in aqueous solution: a biomimetic mineralization study. *European Journal of Mineralogy*, **27**, 717–729 (2015).
44. Kimura, T. & Koga, N. Monohydrocalcite in comparison with hydrated amorphous calcium carbonate: precipitation condition and thermal behavior. *Crystal growth & design*, **11**, 3877–3884 (2011).
45. Kimura, T. & Koga, N. Thermal dehydration of monohydrocalcite: overall kinetics and physico-geometrical mechanisms. *The Journal of Physical Chemistry A*, **115**, 10491–10501 (2011).
46. Koga, N., Nakagoe, Y. & Tanaka, H. Crystallization of amorphous calcium carbonate. *Thermochim. Acta*, **318**, 239–244 (1998).
47. Reeder, R. J. *et al.* Characterization of structure in biogenic amorphous calcium carbonate: Pair distribution function and nuclear magnetic resonance studies of lobster gastrolith. *Crystal growth & design*, **13**, 1905–1914 (2013).
48. Köll, P., Borchers, G. & Metzger, J. Thermal degradation of chitin and cellulose. *Journal of Analytical and Applied Pyrolysis*, **19**, 119–129 (1991).
49. Leontyev, D. V., Schnittler, M., Stephenson, S. L. & Novozhilov, Y. K. Shchepin, O. N. Towards a phylogenetic classification of the Myxomycetes. *Phytotaxa*, **399**, 209–238 (2019).
50. Ishii, Y., Nishiwaki, Y., Al-zubaidi, A. & Kawasaki, S. Pore size determination in ordered mesoporous materials using powder X-ray diffraction. *The Journal of Physical Chemistry C*, **117**, 18120–18130 (2013).
51. Garvie, L. A. J., Knauth, L. P., Bungartz, F., Klonowski, S. & Nash, T. H. Life in extreme environments: survival strategy of the endolithic desert lichen *Verrucaria rubrocincta*. **95**, 705–712 <https://doi.org/doi:10.1007/s00114-008-0373-0> (2008).
52. Verchovsky, A. B., Anand, M., Barber, S. J., Sheridan, S. & Morgan, G. H. A quantitative evolved gas analysis for extra-terrestrial samples. *Planetary and Space Science*, **181**, 104830 (2020).

Tables

Table 1

Major element compositions (wt%) for two FSW and one FSY HACCC samples, and for monohydrocalcite. Additional compositional details are in Tables S1 and S2.

Major Element (wt%)							
	Ca _P	M _{tot-TG}	Mn _P	O _{dif}	C	H	N
FSW21	30.5 (n=3)	31.9	0.12	53.375	12.49	2.505	1.01
FSW22	32.4 (n=3)	n.d.	0.12	52.115	12.145	2.350	0.87
FSW _{avg}	31.5 (31.5±1.5)	-	0.12	52.745	12.32	2.428	0.94
FSY1	28.1 (n=2)	31.92	3.33 (n=2)	49.84	14.63	2.62	1.50
Monohydro- calcite	33.94	-	-	54.19	10.17	1.71	-

P – PIXE. M_{tot-TG} – total metal wt% determined by TG assuming that the product after heating to 1000°C is (Ca, Mn)O only. O_{dif} - oxygen determined by the difference of other measured elements. C, H, N by bulk CHN analysis. n.d. - not determined

Figures

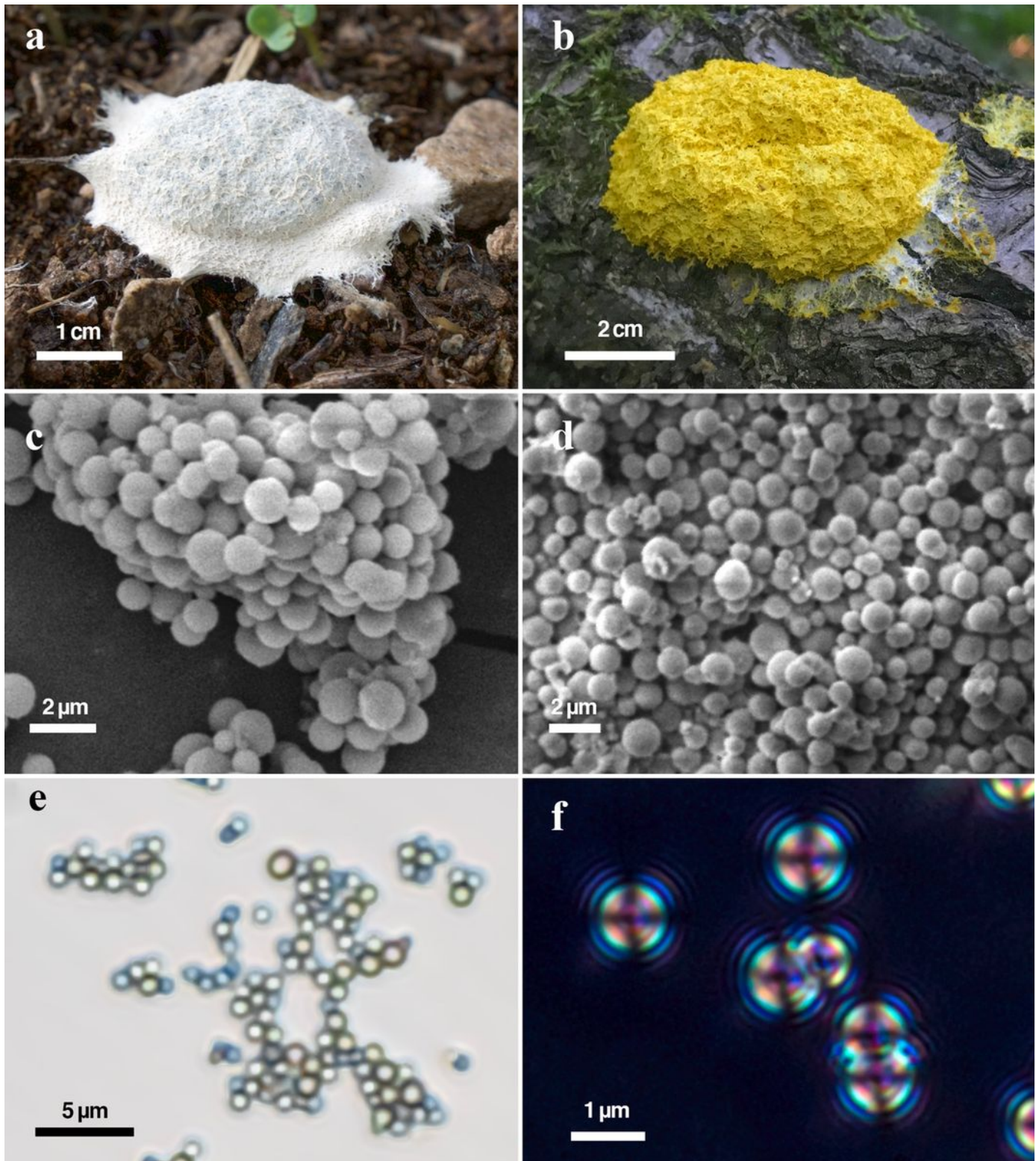


Figure 1

Photographs of *Fuligo septica aethalia* of (a) typical Arizona specimen (FSW), and (b) yellow specimen from the UK (FSY), and corresponding BSE SEM images of the peridium (c, d) showing the fundamental spherical morphology of the peridial HACC. (e) Optical transmitted light microscope image of a cluster of HACC spheres, and (f) crossed-polarized transmitted light optical image of the spheres. The spheres show dark isogyres and isochromatic rings characteristic of an amorphous material.

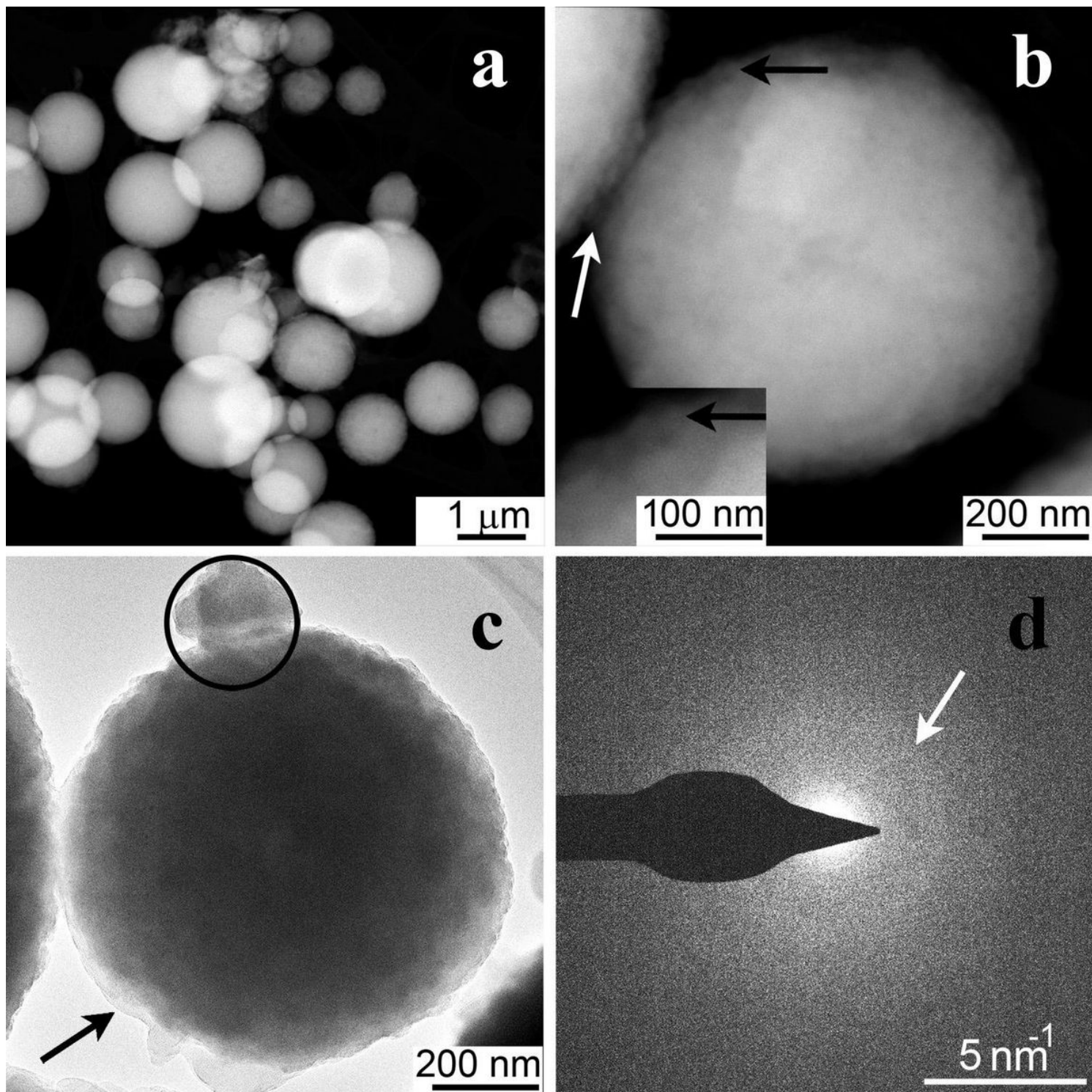


Figure 2

Morphology and structure of the FSY HACC precipitated by *Fuligo septica*. (a) Low-magnification HAADF-STEM image of the peridial HACC spheres. (b) HAADF-STEM and (c) BFTEM images of one sphere. Black arrow marks ~ 30 - 40 -nm size quasi-spherical features. Imaged processed to more clearly reveal the internal clumping is shown in Fig. S3. (d) SAED pattern acquired from the circled area of (c). White arrow points to a diffuse diffraction ring with $d \sim 0.29$ nm spacings.

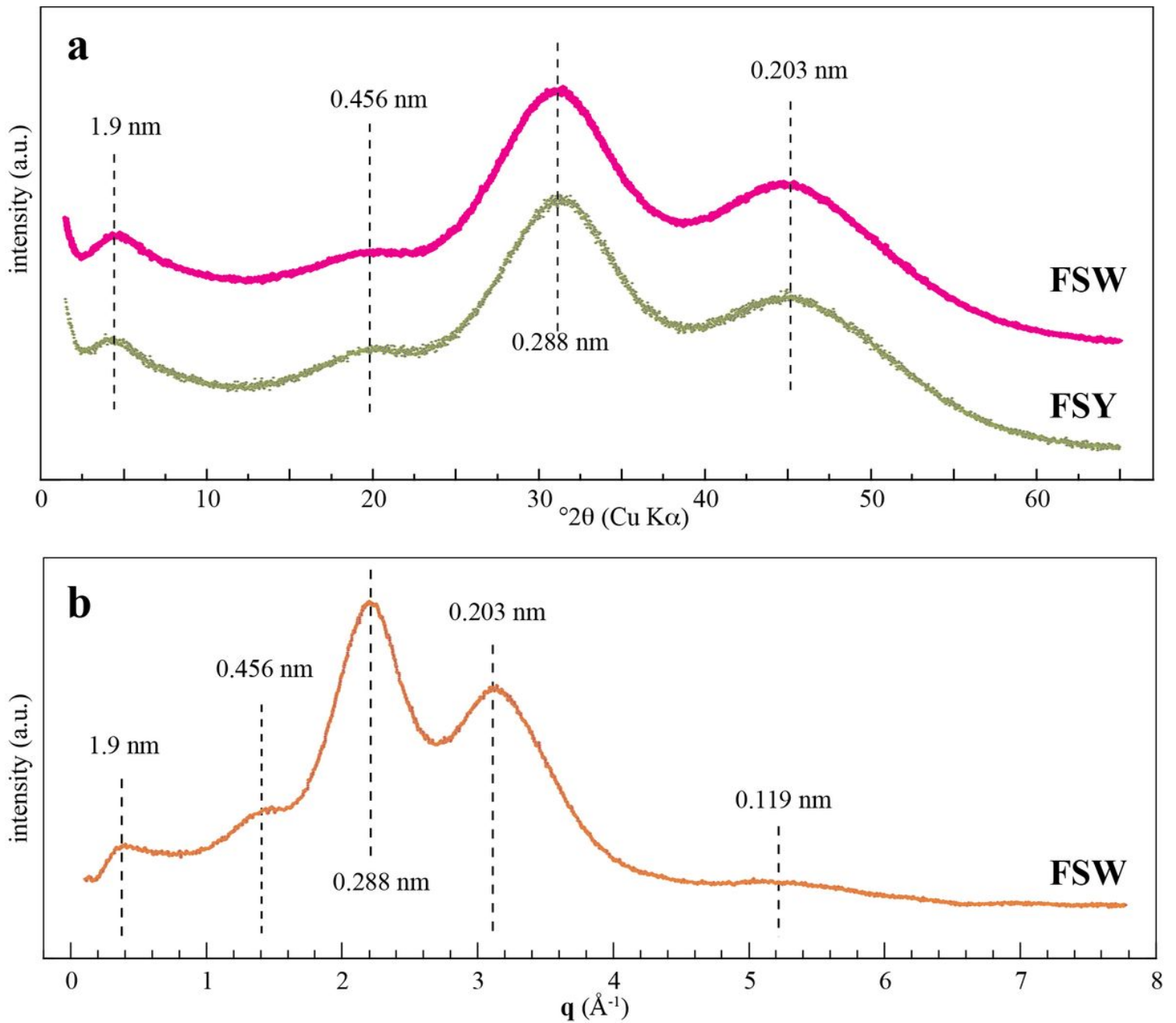


Figure 3

Powder x-ray diffraction patterns from representative HACC samples from the Arizona (FSW) and UK (FSY) *Fuligo septica* peridia. The FSY pattern is from the same aethalia shown in Figure 1b. (a) Raw powder x-ray diffraction patterns. (b) X-ray diffraction pattern from FSW after background subtraction and intensities plotted as a function of scattering vector q (\AA^{-1}).

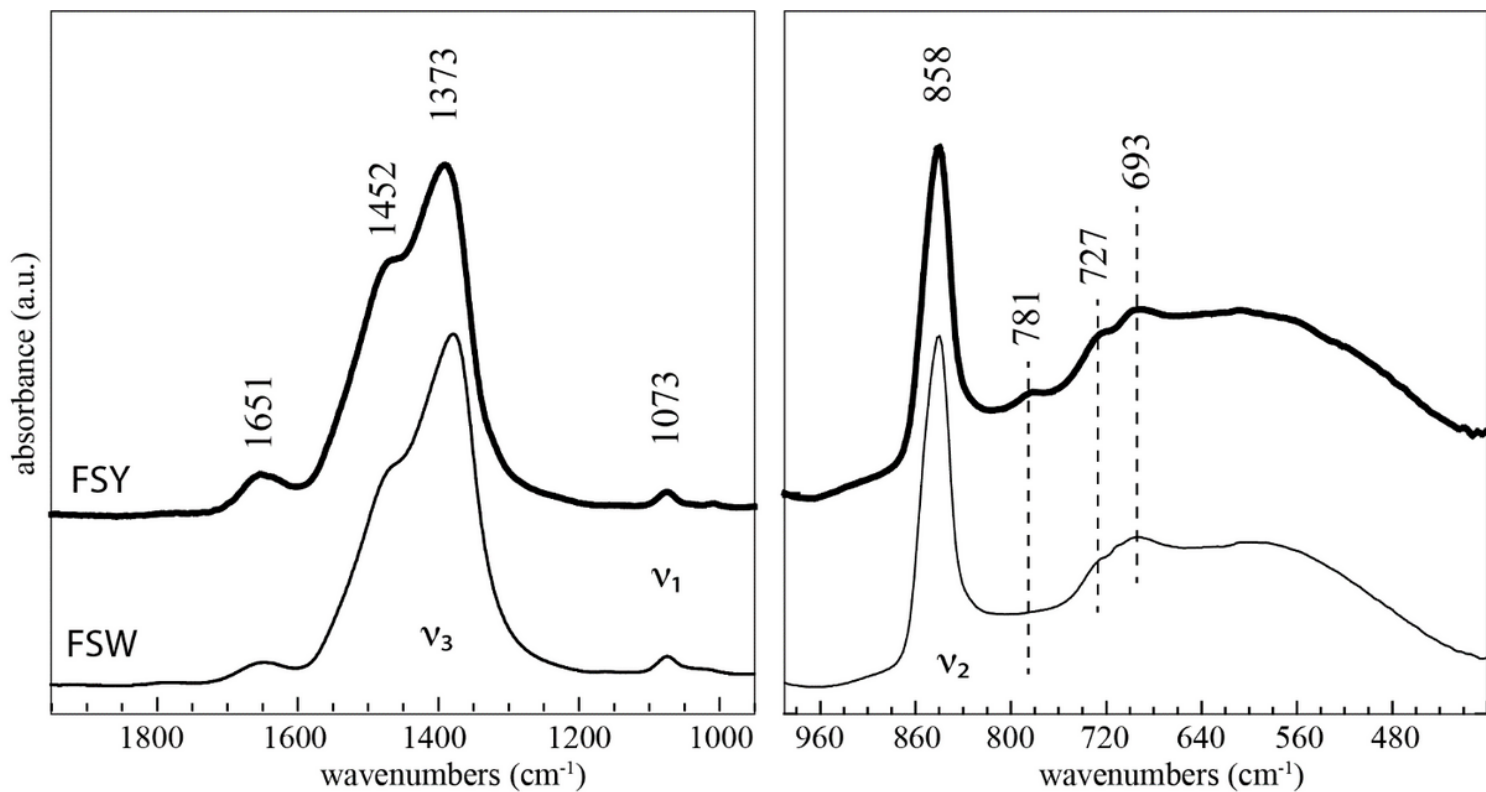


Figure 4

Selected regions of the IR spectra of FSY (sample FS1) and FSW (sample FSW4) HACCC acquired at room temperature. Full spectra are shown in the supplementary information (Figs. S4, S16).

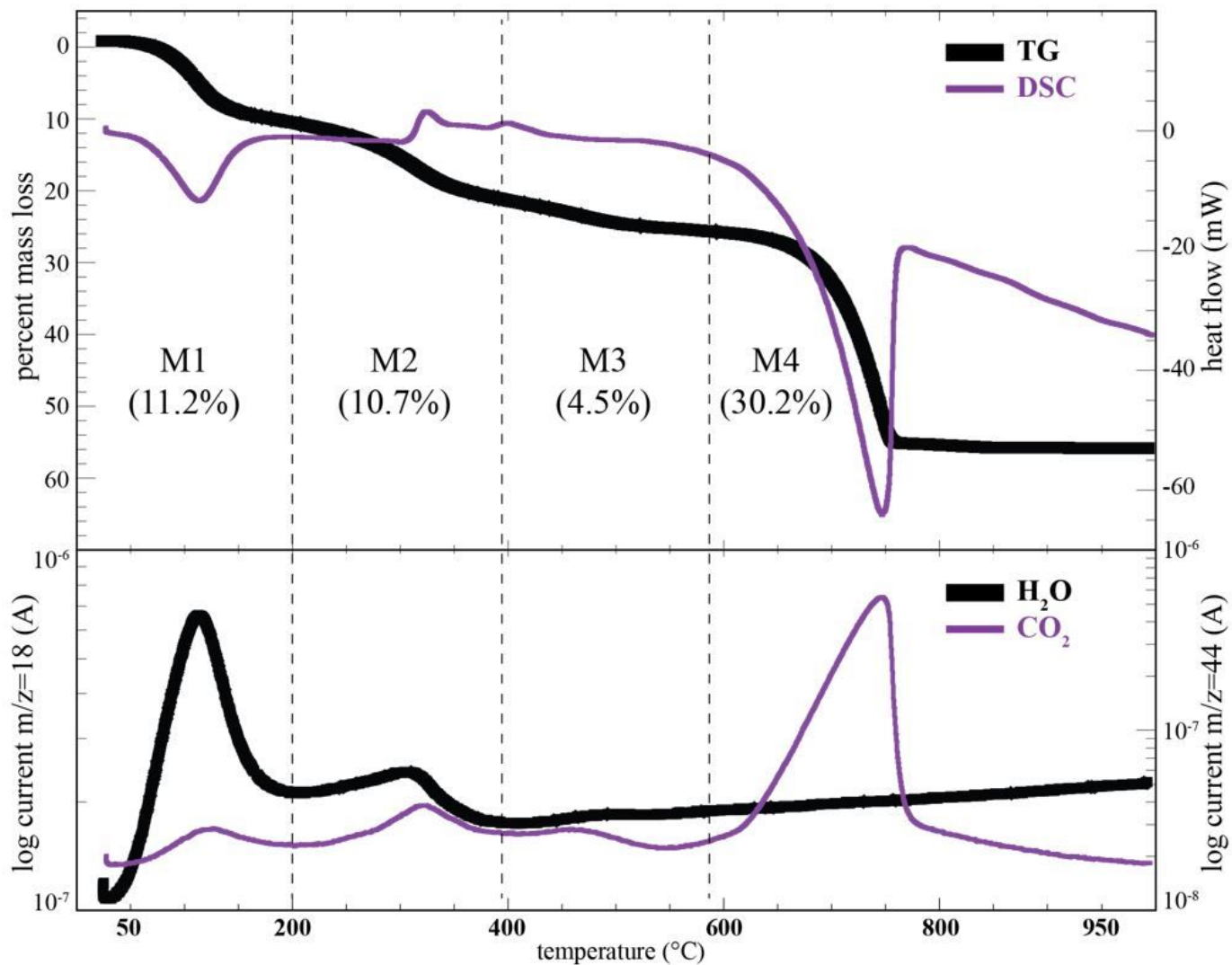


Figure 5

Thermal (TG and DSC) and EGA data for the FSY HACC. M1 to M4 refer to the four distinct mass-loss ranges discussed in the text, and the corresponding percent mass loss within each range in parentheses. The EGA data show the curves for m/z=18 (H₂O⁺) and m/z=44 (12CO₂⁺).

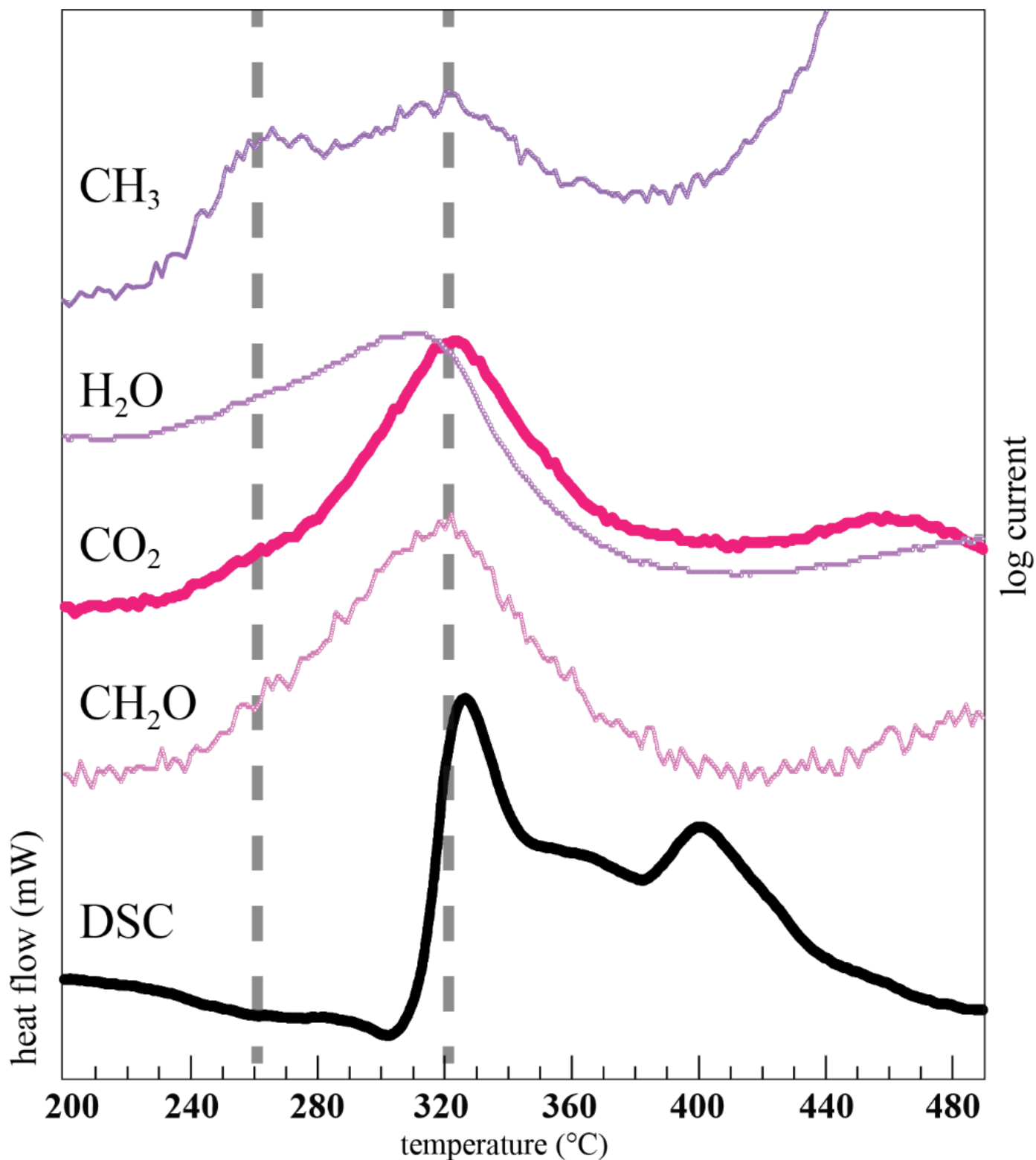


Figure 6

Comparison of the exothermic DSC region (in mW) for the FSY sample run under He (bottom curve) compared with selected EGA profiles (ion current) corresponding to CH₂O⁺ (m/z=30), ¹²CO₂⁺ (m/z=44), H₂O⁺ (m/z=18), and CH₃⁺ (m/z=15). Additional gas assignments are listed in the figure caption for Figure S10. All profiles are scaled and shifted along the y-axis so as to show the correspondence between the peak maxima. The absolute EGA scales are shown in Figure S10.

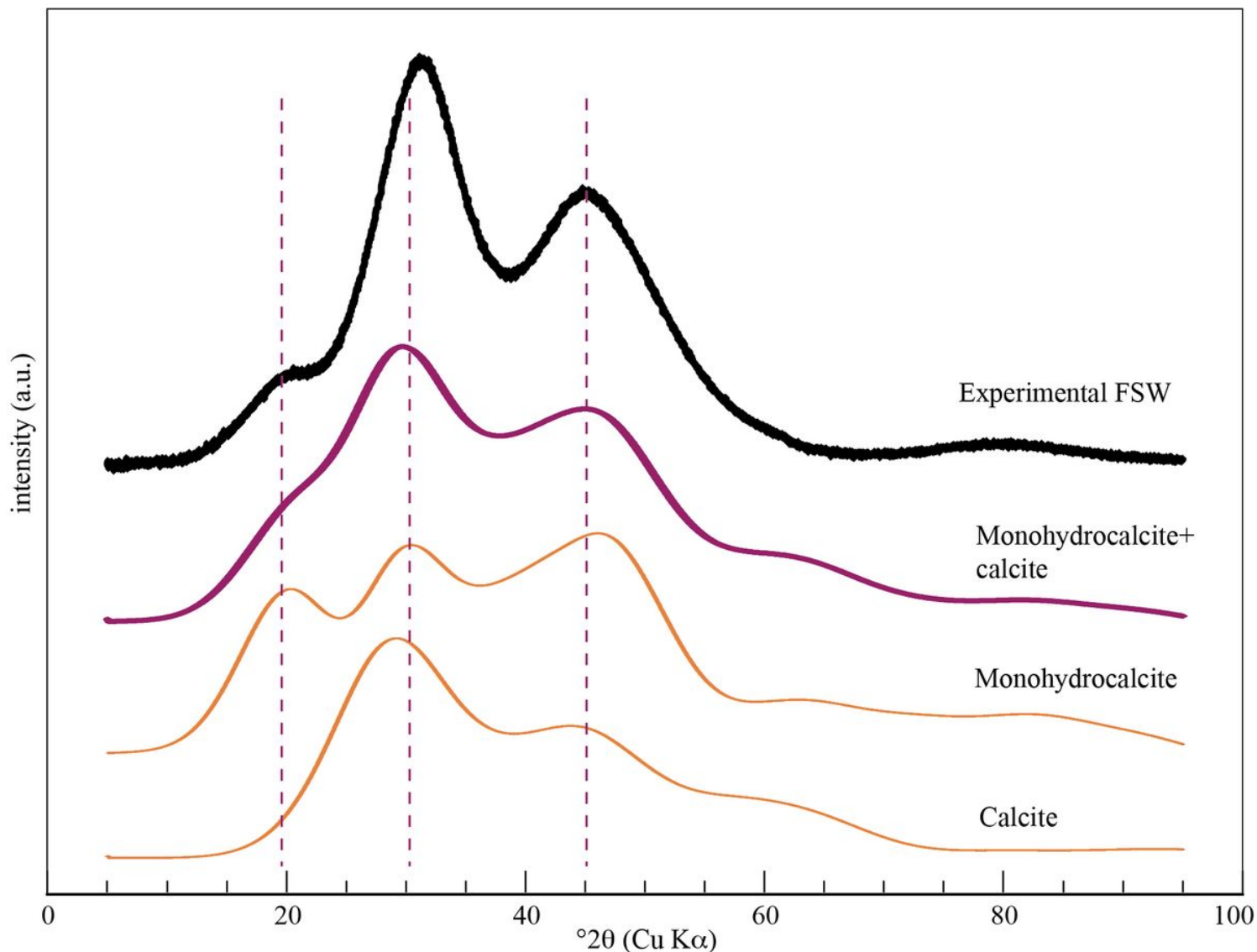


Figure 7

Comparison of the experimental XRD diffraction profile for the FSW HACCC compared with simulated patterns for 0.8-nm calcite, 1-nm monohydrocalcite, and a linear sum of the two (Monohydrocalcite+calcite). The measured background below the experimental pattern has been subtracted as well as the contribution from the 1.9 nm peak.

Supplementary Files

This is a list of supplementary files associated with this preprint. Click to download.

- [slimemoldpapersuppl.docx](#)